JGR

RESEARCH ARTICLE

Correspondence to:
J. G. Frank,
jgfrank111@gmail.com

Shear wave seismic interferometry for lithospheric imaging: Application to southern Mexico

J. G. Frank[1,2], E. N. Ruigrok[1,3], and K. Wapenaar[1]

[1]Department of Geoscience and Engineering, Delft University of Technology, Delft, Netherlands, [2]Now at Shell Canada Limited, Calgary, Alberta, Canada, [3]Now at Department of Earth Sciences, Utrecht University, Utrecht, Netherlands

Abstract Seismic interferometry allows for the creation of new seismic traces by cross correlating existing ones. With sufficient sampling of remote-source positions, it is possible to create a virtual source record by transforming a receiver location into a virtual source. The imaging technique developed here directly retrieves reflectivity information from the subsurface. Other techniques, namely receiver-function and tomography, rely on mode-converted energy and perturbations in a velocity field, respectively, to make inferences regarding structure. We select shear phases as an imaging source because of their lower propagation velocity, sensitivity to melt, and ability to treat vertical shear and horizontal shear wavefields independently. Teleseismic shear phases approximate a plane wave due to the extent of wavefront spread compared to a finite receiver array located on the free surface. The teleseismic shear phase transmission responses are used as input to the seismic interferometry technique. We create virtual shear source records by converting each receiver in the array into a virtual source. By cross correlating the received signals, the complex source character of distant earthquakes is imprinted on the virtual source records as the average autocorrelation of individual source-time functions. We demonstrate a technique that largely removes this imprint by filtering in the common-offset domain. A field data set was selected from the Meso-America Subduction Experiment. Despite the suboptimal remote-source sampling, an image of the lithosphere was produced that confirms features of the subduction zone that were previously found with the receiver-function technique.

1. Introduction

Frequently employed lithosphere imaging techniques include the construction of receiver functions (RFs) and body wave tomography. RFs rely on mode-converted energy from subsurface interfaces near the receiver to provide arrival time differences that can be related to lithology contrasts. Body wave tomography requires inversion of arrival time data to determine perturbations in a velocity field from a background model. Both techniques have advantages and disadvantages. RFs are capable of determining the relative positions of interfaces in the subsurface, but average structure over a large number of conversion points. With RFs, the upper mantle region is difficult to image due to free-surface-reflected phases. Tomographic techniques produce useful velocity information but require condition and resolution parameterization to solve an ill-posed problem. We develop a technique that images the lithosphere by directly recovering reflectivity information from the subsurface through seismic interferometry (SI). This technique is particularly advantageous for imaging strong velocity and density contrasts in the upper mantle, limited only by the recovered bandwidth and ray parameters in a well-sampled data set.

SI exists in a variety of mathematical forms to address a variety of applications [e.g., *Lobkis and Weaver*, 2001; *Derode et al.*, 2003; *Snieder*, 2004; *Wapenaar et al.*, 2004]. Many of the uses of SI focus on the ability to create new seismic traces by cross correlating received signals recorded at separate locations. The sum of this operation, for multiple sources, results in the creation of a new signal such that one of the recording locations acts as a virtual source to the remaining receivers. This technique bears similarities to earlier imaging techniques that also rely on free-surface reflections of body waves for imaging, such as pioneering work by *Bostock et al.* [2001]. However, in the technique presented here, isolating the backscattered energy from the transmission response is performed automatically through cross correlation and stacking within the SI process. The mechanism and related theory employed in this paper are described in detail in *Wapenaar et al.* [2010a]. With many receiver positions available and sufficient source sampling, it is possible to produce a virtual source record (VSR) as if a source is present at one of the receiver positions. By locating
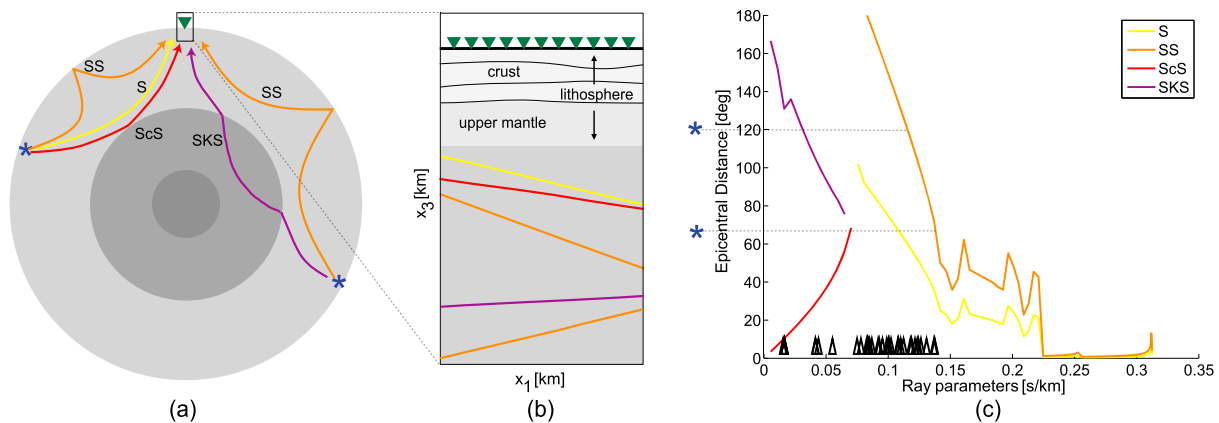
Figure 1. (a) The generation of multiple *S* wave phases from individual earthquakes. The paths that the phases take from the source location to a receiver array are shown as ray approximations. (b) The same phases, each sampling a unique ray parameter, now approximated as plane waves on the local scale of the receiver array. Axis labels x_1 and x_3 refer to lateral distance and depth, respectively. (c) The relationship between epicentral distance and possible ray parameter sampling. In Figure 1c, we also add black tick marks for the actual ray parameters sampled in the Meso-America Subduction Experiment (MASE) field data set used in the imaging experiment.

the virtual source position at an existing receiver coordinate, the VSR produced directly reveals reflectivity from the subsurface. On a synthetic data set, we show how to create VSRs from teleseismic shear phase transmission responses.

Shear waves are desirable for imaging due to the relatively low velocity with which they propagate through the lithosphere, an increased sensitivity to melt, and the potential for separate treatment of the S_V and S_H fields. We select earthquakes at teleseismic distances for primarily two reasons: (a) at large offsets, the incoming energy approximates a plane wave due to the spread of the wavefront in relation to the comparatively finite seismic array, and (b) long epicentral offsets act as a natural temporal filter to separate the incident *P* and *S* wave arrivals. Here "teleseismic events" refers to seismic events originating at greater than 30° epicentral distance. We also anticipate to benefit from the unique ray parameters sampled by each of the various *S* wave phases (i.e., *S*, *SS*, *ScS*, *PS*, and *SKS*). A similar implementation for *P* wave phases was developed in *Ruigrok et al.* [2010]. As depicted in Figure 1, multiple ray parameters may be sampled with a single earthquake through the generation of multiple *S* wave phases. This figure also illustrates how a teleseismic source approximates a plane wave by the time it reaches the local recording array.

Earthquake sources present practical obstacles for imaging, including the complex source signature of earthquake events and imperfect techniques for distilling the *S* and *P* wavefields at the receiver. We refer to the complex source character and source-side reverberations (depth phases) that imprint on the transmission responses as the source-time function (STF). Removal of the majority of this imprint is possible as is demonstrated later. Separating the majority of *S* and *P* wave energy is possible by selecting teleseismic sources (which allow the *S* and *P* wave energy to separate temporally) and by applying receiver-side decomposition. Once a series of VSRs are created, after appropriate preprocessing, conventional imaging techniques may be used to create an image from the resulting data set.

To demonstrate this technique on a field data set, we image a portion of the Cocos subduction zone beneath southern Mexico. The Mexican subsurface is an interesting area to apply this imaging technique. The subsurface features a subducting slab with an extensive tear and changes in dip, including a large horizontally migrating section, in a region affected by earthquakes, volcanism, and nonvolcanic tremors. [*Payero et al.*, 2008; *Pérez-Campos et al.*, 2008; *Chen and Clayton*, 2009; *Husker and Davis*, 2009; *Kim et al.*, 2010]. A data set is selected with sufficient surface coordinate sampling and plentiful earthquake recordings. The Meso-America Subduction Experiment [*MASE*, 2007] array spans over 500 km from Acapulco on the southern coast toward the town of Tempoal in the north. With 100 receiver stations, the average receiver spacing is approximately 5–6 km. Previous studies in the region offer insight into the region through the use of RFs [*Pérez-Campos et al.*, 2008; *Kim et al.*, 2010], tomography [*Husker and Davis*, 2009], and receiver-side reverberations [*Kim et al.*, 2012]. The MASE data set has been publicly available for a number of years, which provides several publications to compare the results of shear wave SI to.

2. Foundation

2.1. Seismic Interferometry

For a more thorough introduction to SI theory and applications, we again refer the reader to *Wapenaar et al.* [2010a, 2010b, and the many references therein]. The elastic Green's function representation that provides the basis for this work is reprinted from *Draganov et al.* [2006];

$$G_{n,q}^{\upsilon,\tau}(\mathbf{x}_B, \mathbf{x}_A, t) + G_{n,q}^{\upsilon,\tau}(\mathbf{x}_B, \mathbf{x}_A, -t) \approx \frac{2}{\rho c^K} \int_{\partial S_1} G_{n,K}^{\upsilon,\phi}(\mathbf{x}_B, \mathbf{x}, t) * G_{q,K}^{\upsilon,\phi}(\mathbf{x}_A, \mathbf{x}, -t) \mathrm{d}^2\mathbf{x}. \tag{1}$$

The Green's function is written as a function of receiver location, source location, and time (first, second, and third entries within the parenthesis, respectively). The receiver and source type are expressed with superscripts and subscripts, in the same order as the location vectors between the parentheses. The left-hand side of the equation represents the retrieved Green's function in terms of particle velocity (υ) at $\mathbf{x}_B$ due to an impulsive traction source (τ) at $\mathbf{x}_A$; both the causal and acausal (time-reversed) responses are retrieved. Here subscript n represents the direction of particle velocity of the received response at $\mathbf{x}_B$. A traction source oriented in the direction of subscript q is located at position $\mathbf{x}_A$. For the retrieved Green's function, both the receivers and sources are located on the free surface. The right-hand side Green's functions represent the particle velocity observations due to an impulsive source at $\mathbf{x}$; $\mathbf{x}$ denotes a location on ∂S_1, which spans an open boundary in the subsurface. The "$*$" symbol denotes convolution of the Green's functions; because one of the Green's functions is reversed in time this comes to a correlation. Here ϕ represents a P wave source when $K = 0$ or one of the three orthogonal S wave source polarizations for $K = 1, 2,$ and 3. Similarly, c^K represents the propagation velocity of the corresponding wave, and ρ represents the density. Einstein's summation convention applies to repeated Latin subscripts. Note that the derivation in *Draganov et al.* [2006] expands on previous work by *Wapenaar and Fokkema* [2006] where approximations, primarily regarding amplitude, are employed.

We utilize equation (1) for a scenario where teleseismic transmission responses (the right-hand side of equation (1)) are used to retrieve a reflection response from receivers on the surface (the left-hand side of equation (1)). For our purpose, we apply further approximations to equation (1) with the goal of representing the two shear wavefields (S_V and S_H) as independent scalar fields. As mentioned previously, for teleseismic sources, the Earth acts as a temporal filter for separating the incident P and S wave energy due to the differences in propagation velocity. By the time an S wave phase arrives, any remaining P wave energy is greatly attenuated compared to the energetic S wave arrival. Thus the primary contribution of P wave energy remaining in the system is from SP mode conversions. For low ray parameters, the P, S_V, and S_H fields map primarily to the vertical, radial, and transverse components, respectively. Large ray parameters require decomposition to isolate the S_V contribution. By selecting seismic events within a narrow azimuthal range along the direction of the seismometer array and receiving near-planar wavefields, we may apply a 2-D approximation to equation (1). We further rewrite the expression to accommodate the transition from point sources to plane wave sources [*Ruigrok et al.*, 2010] and formulate the S_V expression as

$$G_{S_V}(\mathbf{x}_B, \mathbf{x}_A, t) + G_{S_V}(\mathbf{x}_B, \mathbf{x}_A, -t) \propto \int G_{S_V}(\mathbf{x}_B, p, t) * G_{S_V}(\mathbf{x}_A, p, -t) \mathrm{d}p, \tag{2}$$

where p is the incident ray parameter and all Green's functions denote responses as if there were S_V sources and S_V receivers. Equation (2) does not account for SP-converted energy that may be converted back to S waves. Mode-converted SP energy is typically low in comparison to dominant S wave amplitude, so any energy present through subsequent PS conversion may be neglected. A similar formulation in terms of the S_H field may also be created; in this case, an added benefit is that mode-converted energy is not a concern. In the case of 3-D structure, the S_H contribution could couple with other modes present, leading to small artifacts in the SI result as we implement it.

The functions under the integral in equation (2) (and its S_H analog) represent the teleseismic transmission responses of S wave phases recorded at two receiver locations ($\mathbf{x}_A$ and $\mathbf{x}_B$) within an array. In practice, the integral is not continuous; rather, discrete transmission responses are available within a given data set. To
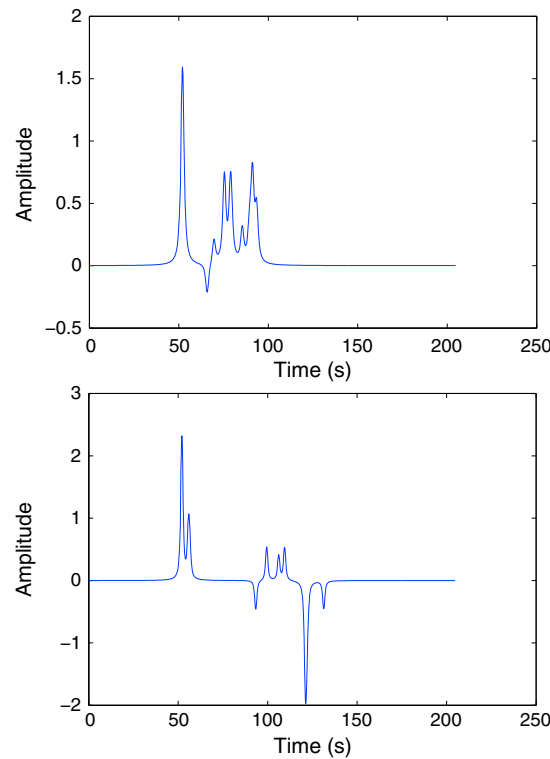
Figure 2. Two generated STFs are shown. Note the variability in the number of reverberations (small-amplitude peaks and troughs) and trailing larger-amplitude reverberations from free-surface reflections (depth phases). The time scale is shown in seconds, demonstrating the period over which energy is distributed.

obtain a sufficient sampling in ray parameter, we combine the discrete version of equation (2) with its S_H analog, yielding

$$G_S(\mathbf{x}_B, \mathbf{x}_A, t) + G_S(\mathbf{x}_B, \mathbf{x}_A, -t)$$
$$\propto \sum_{p_{min}}^{p_{max}} G_{S_V \vee S_H}(\mathbf{x}_B, p, t) * G_{S_V \vee S_H}(\mathbf{x}_A, p, -t) \Delta p.$$
(3)

Combining cross correlations of S_H and S_V wavefields further deteriorates the interpretability of the amplitudes of the retrieved Green's function $G_S(\mathbf{x}_B, \mathbf{x}_A, t)$, which is an average over S_H and S_V impulse responses. Besides, there may be small kinematic differences between S_H and S_V due to anisotropy, but in the absence of strong anisotropy, the shift in arrival times between S_H and S_V waves is expected to be relatively small compared to the wavelengths of the low frequencies received at the surface. Therefore, it is expected that S_H and S_V cross correlations still contribute constructively to the above summation. The available sources range in ray parameters from p_{min} to p_{max}; for teleseismic events, these values lie between −0.14 and +0.14 s/km as seen in Figure 1c.

With sufficient sampling by a finite number of sources with comparable bandwidths, reflectivity retrieved by SI will reach stationarity in the cross-correlation process [*Snieder*, 2004] allowing the creation of a virtual source. By successively applying equation (3) for a fixed virtual source position $\mathbf{x}_A$ and varying auxiliary receiver $\mathbf{x}_B$, a complete VSR is obtained. Moreover, with all receivers assuming one-by-one the virtual source role in individual VSRs, enough records become available to apply seismic reflection imaging.

2.2. Source Character Imprint and Removal

The STF character generated by an earthquake is complex and has a large imprint on the (receiver-side) transmission response. To develop a technique that can remove the effect of the STF, we construct a model based on the Haskell source (a discussion of this topic can be found in *Stein and Wysession* [2009]). The duration of the initial STF pulse is taken as the convolution of two box-car functions. One of these box-car functions represents the rise time T_D; this is understood as the duration of the slip at one position in space. The second box-car function represents the rupture time T_R, which is the time difference (as observed by the receiver) of the start of the slip at the nucleus position and the start of the slip at the final reach of the rupture. We also consider other properties influencing the STF. Source-side reflections from the free surface are modeled; one reflection representing the *sS* phase and another, with smaller delay time and lower amplitude, the *pS* phase. To these source-side reverberations, we add additional low-amplitude reverberations to model wavefield modulation by source-side material contrasts other than the free surface. We also allow variation in source depth, which influences the temporal duration of the resulting STF. Reverberations by the mantle and core regions are not considered as they are relatively homogeneous in comparison to near-source features. Attenuation is determined by travel time and an average Q factor for mantle materials. Temporal separation of the source-side reverberations are modulated by an event depth parameter. These factors are combined to generate STFs that reasonably simulate the potential complexity of a field recording; Figure 2 shows two random STFs generated by this method. The imprint of an STF on a transmission response is shown in the modeling results section later.

Removal of the STF is not a straightforward matter. The STF is not minimum phase (i.e., the STF does not contain a causal and stable inverse), which impairs our ability to design a well-behaved filter, thereby

making conventional deconvolution techniques unusable (for more details on this topic, please refer to *Yilmaz* [2001]). Explicit removal of the STF from the transmission response after cross correlation (within the SI process) also fails; the STF imprint overlaps with reflectivity information due to its long duration (Figure 2). In the following, we develop a technique that utilizes the consistent behavior of the average STF autocorrelation over the array to provide a means for suppression.

We rewrite the Green's functions in equation (3) into transmission and reflection responses, as in *Wapenaar* [2003]. Thus, we implicitly assume a configuration for which wavefields can be separated in upgoing and downgoing components. Additionally, we convolve the transmission responses with STFs, yielding

$$\left\{ -R_S(\mathbf{x}_B, \mathbf{x}_A, -t) - R_S(\mathbf{x}_B, \mathbf{x}_A, t) \right\} * S_N(t) + \text{SDW} \propto \sum_{p_{\min}}^{p_{\max}} T_{S_V \vee S_H}(\mathbf{x}_A, p, -t) * s_i(-t) * T_{S_V \vee S_H}(\mathbf{x}_B, p, t) * s_i(t) \Delta p, \quad (4)$$

where $T_{S_V \vee S_H}(\mathbf{x}_A, p, t)$ is the transmission response for a plane wave with ray parameter p (from either a S_V or S_H wave) detected at $\mathbf{x}_A$, $R_S(\mathbf{x}_B, \mathbf{x}_A, t)$ is an average over the S_H and S_V reflection response between two surface positions and $s_i(t)$ is the STF of a transmission response. Cross correlating and stacking observed transmission responses again yields the reflection response and its time-reversed version, but additionally there is now a convolution with an average over STF autocorrelations, $S_N(t)$, and there are two additional terms that are spurious direct waves (SDW). For our case, we write

$$\text{SDW} \propto \left\{ \delta(t - (\mathbf{x}_{1,B} - \mathbf{x}_{1,A})p_{\max}) + \delta(t - (\mathbf{x}_{1,B} - \mathbf{x}_{1,A})p_{\min}) \right\} * S_N(t), \quad (5)$$

assuming the x_1 axis is defined along the receiver array.

Rewriting the retrieved Green's functions in terms of reflection responses and summing over a limited ray parameter range gave rise to the undesirable SDW. For $p_{\max}$ (and $p_{\min}$) approaching the slowness (and negative slowness) of surface waves, the terms in equation (5) converge to surface-wave arrivals between $\mathbf{x}_{1,A}$ and $\mathbf{x}_{1,B}$. For our configuration, with illumination only from below, the SDW remain spurious, arising from the edges of the summation interval. As the spurious terms arise from cross correlations of waves with the same order (e.g., direct transmission arrivals with direct transmission arrivals), they have much larger amplitude than physically retrieved events, which arise from cross correlations of waves with different order. Convolution of the spurious terms with a long and complicated $S_N(t)$ gives sidelobes that overlap with retrieved reflectivity. As in *Ruigrok and Wapenaar* [2012], we estimate the SDW by sorting the retrieved VSRs into common-offset gathers (COGs). For each trace in a COG, $\mathbf{x}_{1,B} - \mathbf{x}_{1,A}$ in equation (5) is equal and also $S_N(t)$ may approximate to be equal over the array. However, the reflection response for each trace in the COG is different, as the lithosphere is not horizontally layered. Hence, we estimate the SDW as a mean over the COG. By removing this mean value from each trace, the imprint of the STF is radically minimized. A caveat; with this technique, any amplitudes resulting from perfectly horizontal layering will also be reduced. However, even modestly dipping features are preserved (although perhaps with reduced amplitude) and the lithosphere presented in our case is unlikely to have interfaces that are horizontal over the entire profile.

3. Modeling Results

We demonstrate the above theory on a lossless 2-D model with elastic finite-difference wave propagation [*Thorbecke and Draganov*, 2011]. The 2-D model is constructed to resemble a subduction setting similar to the one anticipated in southern Mexico (Figure 3). The model features a primarily horizontal subducting slab that begins to dip steeply into the mantle at 50 km depth. Attached to the subducting slab is an enlarged low-velocity zone (LVZ); in the Cocos subduction zone, a region of low velocity is believed to be present atop the subducting slab, corresponding to a region of low viscosity or low strength from possible dehydration of the material [*Pérez-Campos et al.*, 2008]. The high-velocity subducting slab is surrounded by a lower velocity mantle to represent the cooler, denser oceanic plate moving through a comparatively ductile mantle. The remainder of the mantle features a nonreflective positive velocity gradient with increasing depth. Velocity ranges were also constrained by referring to the model for the neighboring Chilean subduction zone proposed in *Contreras-Reyes et al.* [2012] and computing reasonable S wave analogs. Note, the full
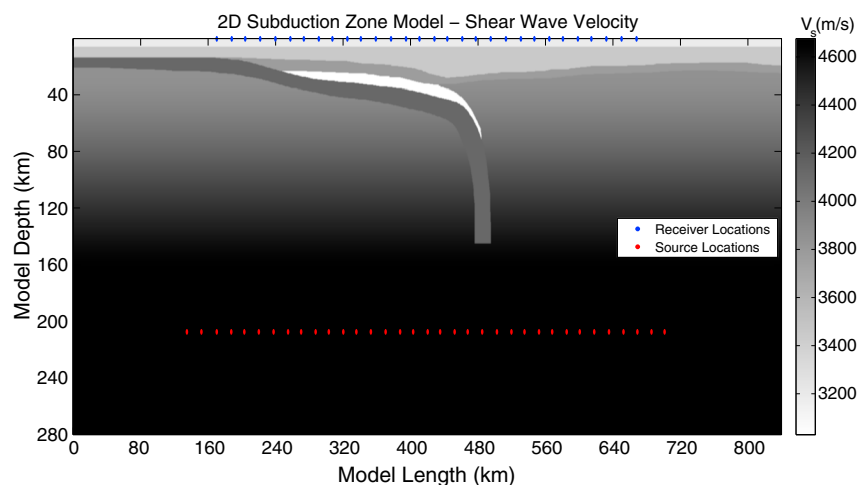
Figure 3. Two-dimensional shear wave subduction model. Receiver positions are indicated in blue, and subsurface source locations are indicated in red. Only one out of every five receiver and source positions used in the modeling is shown to improve image clarity. Shear wave velocities range between 3030 and 4677 m/s.

model is shown in Figure 3, but receivers (in blue) only sample a portion of the model space. For this reason, the images produced from this model show a smaller lateral extent than the full model. A plane wave is simulated by initiating a line of line sources (in red) with delay times pertaining to a certain ray parameter.

A series of plane waves are propagated through the model and recorded at receiver locations on the surface, spanning a total of 500 km with 4 km intervals between stations. A total of 49 unique plane waves are used to sample the model subsurface with values from −0.12 s/km to 0.12 at intervals of 0.005 s/km. During the initial forward modeling, a transient wavelet is used. For each of the 49 transmission responses recorded, the transient wavelet is removed and replaced with a complex and randomly generated STF as described in the previous section. Figure 4 compares a synthetic transmission response with the transient wavelet to one with the STF character, both with a ray parameter value of 0.08 s/km. A sharp decrease in resolution occurs with the lower frequency content, and the source-side reverberations strongly obscure the receiver-side reverberations. The transient wavelet model will serve as a reference case. Receiver-side decomposition is applied to each of the transmission responses to separate S wave energy from SP- converted energy, using the method described in *Kennett* [1991]. Although the STF biases the low end of the frequency spectrum (peaking near 0.05–0.10 Hz), useful imaging energy is contained up to 0.50 Hz in all transmission responses; whitening is applied to each transmission response to balance the bandwidth between 0.01 and 0.50 Hz. The transmission responses are then used as input to the SI algorithm to create VSRs.

Figure 5 shows the VSRs created via SI with (a) the transient wavelet transmission responses, (b) the STF transmission responses, and (c) the STF transmission response after suppression of the STF imprint. All panels use the same virtual source position near the hinge point of the subducting slab. The spurious direct arrival is removed by a top mute in all panels. Features with near-hyperbolic moveout represent reflectivity arising from lithology contrasts. As expected, the reference case using the transient wavelet (Figure 5a) reveals reflectivity with a good resolution. In the case of the STF transmission response (Figure 5b), the reflectivity is difficult to see. The obscuring influence of the STF makes physical features difficult to detect, although some amplitude effects with reflectivity-like character can be seen. By applying the STF imprint removal technique discussed in section 2.2, in Figure 5c, we reveal reflectivity similar to the transient case. Resolution is decreased in the STF case as the bandwidth of all contributing STFs is significantly lower than the transient wavelet. For comparison, the transient wavelet has a dominant frequency of 0.34 Hz, the average STF autocorrelation has a dominant 0.05 Hz. Once the average STF autocorrelation is removed, however, the dominant frequency in the VSR is improved to 0.15 Hz.

We create another VSR data set that utilizes only transmission responses with ray parameters sampled in the field data set. From the field data set, we calculate the ray parameters by global ray tracing. We bin the field data set ray parameters to the closest modeling ray parameters and discard the remainder. This results in
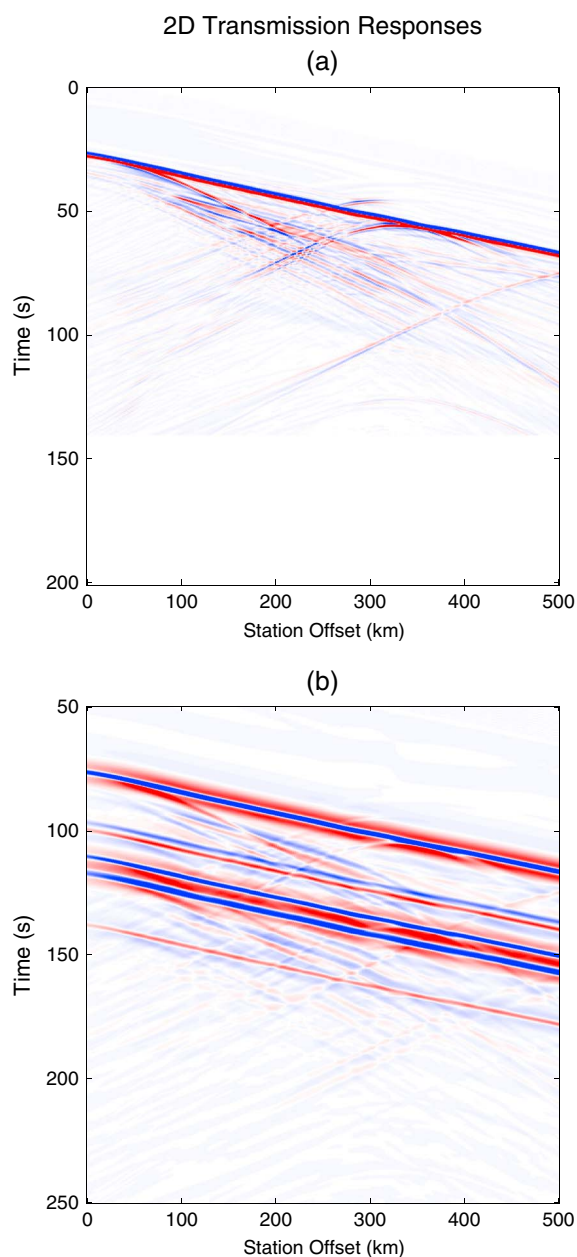
Figure 4. Modeled transmission responses of *S* wave phases received at a surface array (Figure 3). (a) The response to the transient wavelet. (b) A complicated source-time function (akin to Figure 2) convolved with the transmission response. The color scale is normalized on the interval [−1, 1] with red signifying positive polarities.

a total of 16 unique ray parameters, used to create a field-level sampling data set. This field-level sampling data set also undergoes the same STF removal process described in the preceding section.

With three preprocessed data sets available for comparison, namely, the transient case, full sampling STF case, and field-level STF sampling case, we proceed to imaging. A conventional imaging technique (here a Kirchhoff shot migration) is applied to each of the three data sets with a 1-D velocity model, and the image obtained by each shot is stacked to produce a migrated image. Using the same 1-D velocity model, this image is time-to-depth converted to yield the final image. Figure 6 compares the resulting migrations. Figure 6a shows the migration result using the transient wavelet data set (reference case). Figure 6b reveals the migration result obtained by migrating the well-sampled STF VSR data set with full pre- and post-SI processing and common-offset domain filtering to remove the STF imprint. Figure 6c shows the migration result obtained using a field-level sampling STF data set and the same processing steps as in Figure 6b. Note that the edges of the image space are removed to facilitate a comparison of the features of interest. We also include the imaged portion of the input model in Figure 6d. It is clear that the image produced using the unrealistic transient wavelet (Figure 6a) contains the highest resolution; however, all major features present in that fictitious scenario are reproduced (albeit with lower resolution) in the well-sampled STF VSR migration (Figure 6b). The top of the LVZ (strong blue amplitude) is clearly resolved, followed by a positive amplitude from the subducting slab. The abrupt bottom of the slab is even retrieved in both Figure 6a and 6b at 310 km station offset and 145 km depth. Bear in mind that such an abrupt slab bottom is not expected in a field data scenario, but it is encouraging that despite the complications arising from our synthetic STFs
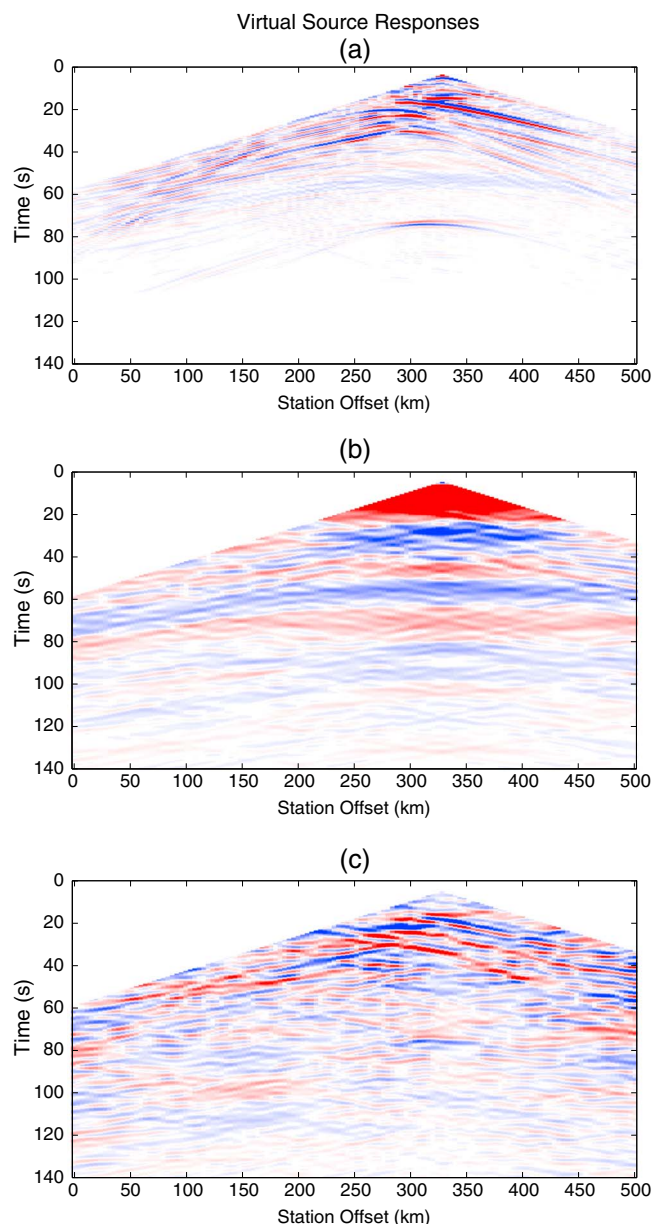
we are still able to resolve this detail from the model. Although the field-level sampling migration (Figure 6c) is of lower quality yet, it offers interpretable value for delineating the subducting slab and hinge region. In all cases, resolving steep dips is limited by the magnitude of available ray parameters. Greater absolute *p* values would allow resolution of steeper dips, but we are limited by nature to the interval between −0.14 and +0.14 s/km for teleseismic sources. Further processing steps are likely to produce improvement in the final image. No multiple removal techniques are applied in the modeling results although the strong material contrasts near the LVZ and free surface contribute to extra reverberations in the transient wavelet case. In the STF case, multiples are not readily observed and are expected to be weak relative to the primary reflections.

Figure 5. Virtual source responses estimated with shear wave seismic interferometry, using (a) transient-source transmission responses, (b) transmission responses with complicated source-time functions, and (c) as previous, but with the additional postprocessing to suppress artifacts introduced by the long source-time functions. The color scale is normalized on the interval [−1, 1] with red signifying positive polarities.

4. Field Data

The field data set selected for analysis comes from the approximately linear MASE array in southern Mexico. The location of each station is depicted in Figure 7. This temporary array was recording for a period of approximately 2 years, the retrieved data spans from January 2006 until June 2007.

For the purpose of imaging Mexico's subsurface, we restrict the transmission responses to those that offer a meaningful contribution toward the objective. For SI to be applied in our configuration, it is critical that the travel path of the plane wave impinging at the receivers propagate from one station and reflect, via interfaces in the lithosphere, to other stations on the surface. If the plane wave approaches the array from the out-of-plane direction, the energy will not "bounce" between stations and will not sample the subsurface in between. To achieve the desired effect, we restrict the available earthquake source positions to those that are near the great circle path through the array. We limit our search to earthquake epicenters that occur within an azimuth of 30° of the orientation of the great circle path from the array. However, to supplement the limited number of recordings available, we expand the 30° criteria to also accept phases with very small ray parameters initiated by large-magnitude earthquakes. With very small ray parameters, sampling between stations is possible even if the event does not locate near the great circle path that passes through the receivers. A minimum moment magnitude (M_w) of 5.5 is required to provide sufficient energy at the array and a filter is applied to automatically discard lower magnitude events. A number of more energetic earthquakes are also discarded due to insufficient signal-to-noise at the array, which further reduces the number of remaining recordings. With these data set reductions applied, earthquake epicenters available in the final data set are shown in Figure 8. The great circle path through the MASE array is depicted by the red dashed line.

Individual S wave phase transmission responses with sufficient signal-to-noise are retrieved from the catalog of recordings. In total, we retrieve 45 unique S wave phases, sampling p values from −0.12 to 0.14 s/km. Unfortunately, the sampling is not evenly distributed, with dominating clusters forming near −0.12 s/km, −0.5 s/km, and near the positive upper threshold. The sampling available is not ideal, but was the best data set at the time of the study for the combination of adequate receiver sampling and availability
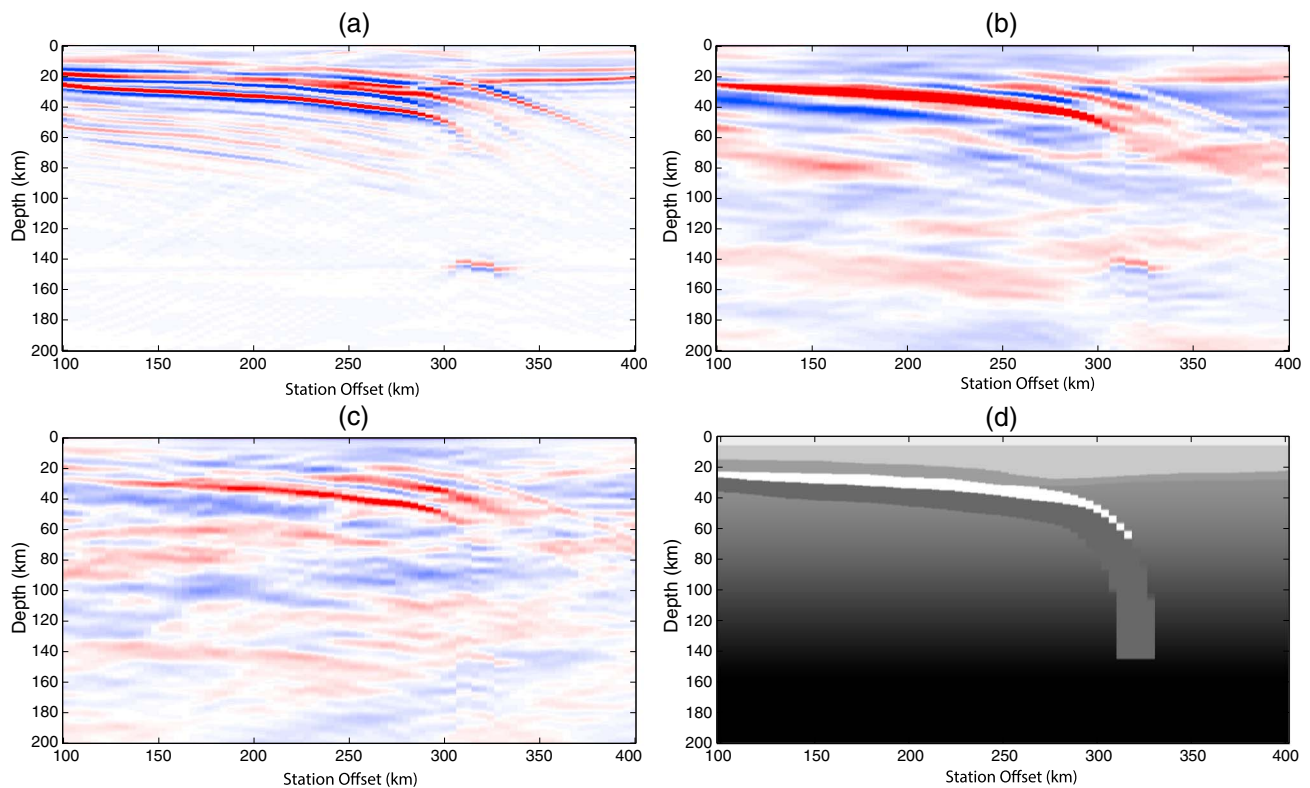
Figure 6. A comparison of migration results with different source-wavelet assumptions, preprocessing, and sampling. Panel (a) shows the SI migration under the transient wavelet assumption, (b) shows the SI STF migration with processing corrections, and (c) shows the SI STF migration result using a field-level of sampling. Panel (d) shows a subset of the 2D velocity model from Figure 3 for comparison. The color scale is normalized on the interval [-1, 1] with red signifying positive polarities.
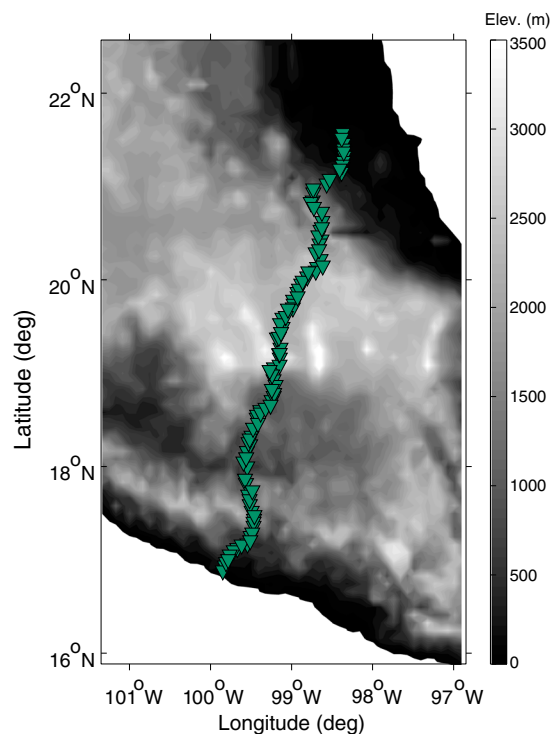

Figure 7. Latitude and longitude of the MASE array stations on a surface elevation plot.

of events. The contribution to the total number of phases comes from both S_V and S_H components. Receiver coordinates are rotated to isolate the majority of the S wave energy to the radial and transverse components. *SKS* and *PS* phases map to the radial receiver component; *S*, *SS*, and *ScS* phases can be detected on both the radial and transverse components. Receiver-side decomposition further improves the separation of the S wave phases from the remaining P wave energy. Although 100 stations are available in total, an average of 70–80 traces remained in the transmission responses once poor quality traces are discarded. Topographic and geometric corrections are applied to each transmission response. Since many of the S wave phases are generated off of the great circle path, a ray parameter correction is applied to each transmission response. Interpolation is used to recover discarded traces as long as spatial aliasing is not a risk.

The transmission responses are then used as input into the SI algorithm. Post-SI corrections, including the suppression of the average STF autocorrelation and the spurious direct arrival,
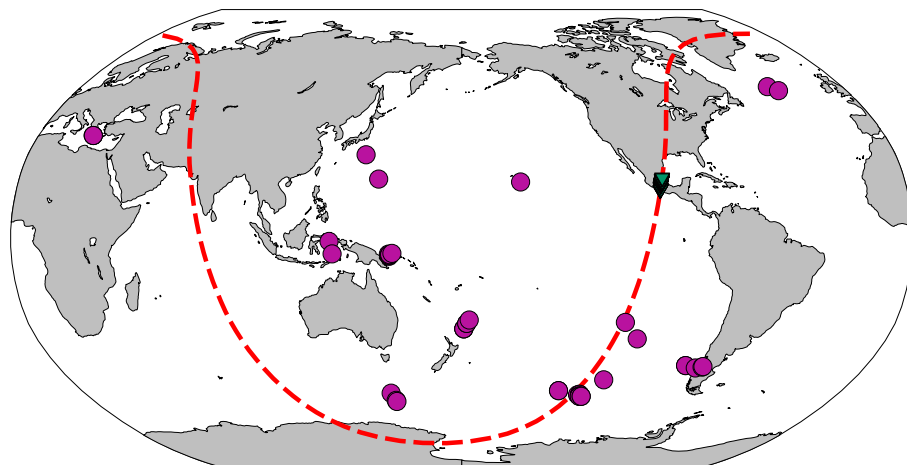
Figure 8. Depiction of the earthquake locations that contribute *S* phase transmission responses to the field data set. While most epicenter locations occur near the great circle path through the MASE array, large-magnitude events which sample low ray parameters away from the great circle path are also included.

are applied. Long offsets are immediately discarded from the data set; beyond 100 km from the virtual source location, signal quality decreases rapidly. Figure 9 depicts the MASE array (a), how the unprocessed VSR relates to the array geometry (b), and how post-SI processing improves the VSR quality (c). Furthermore, additional offsets are discarded from our final data set as a consequence of the suboptimal sampling available. In the final VSRs, only zero-offset retrievals (autocorrelations of recorded phases) are retained and are fed into a 1D surface-related multiple elimination scheme as described in *Verschuur and Berkhout* [1997]. These modified VSRs are used as an input to migration and time-to-depth conversion.

The velocity model used for migrating the data set is a simple 1-D root-mean-square model created by permuting values from the preliminary reference Earth model [*Dziewonski and Anderson*, 1981]. For the top
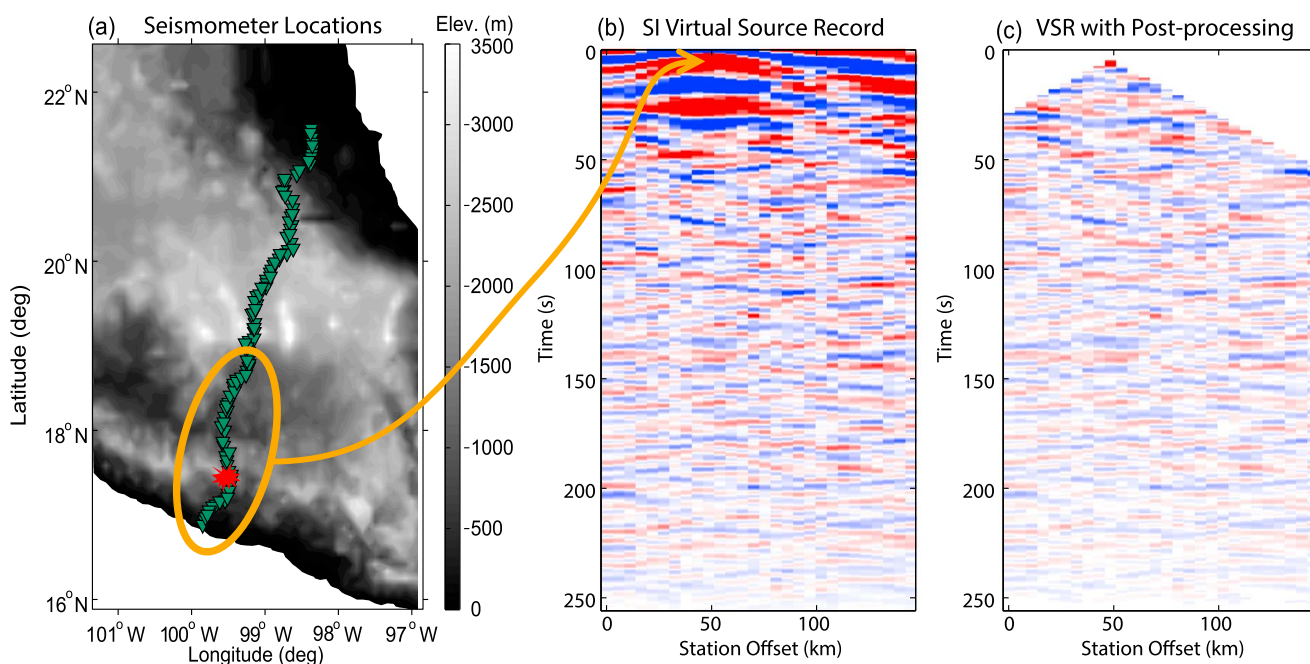

Figure 9. (a) A scenario where a receiver at 54 km acts as a virtual source to the regularized array. (b) The corresponding virtual source response from that virtual source location. (c) The same section of the virtual source record as Figure 9b after post-SI processing. The color scale is normalized on the interval [−1, 1] with red signifying positive polarities.
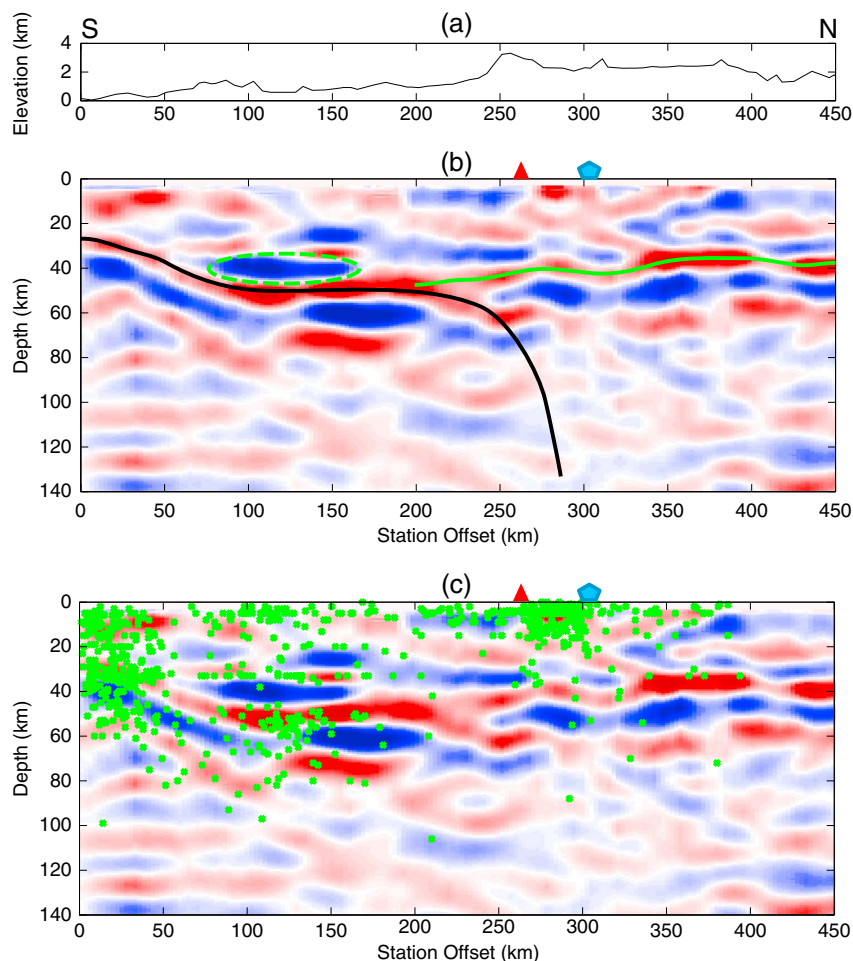
Figure 10. (a) The topography profile of the MASE array along the seismic image. South and north directions are noted at the top of this panel. (b) The migrated image produced from the application of teleseismic shear wave seismic interferometry. The color scale in both Figures 10b and 10c is normalized on the interval [−1, 1] with red signifying positive reflectivity. The black solid line, aligned on the crest of the positive reflector, represents our interpretation of the subducting oceanic crust. The green line represents the location of the continental Moho. The green dashed ellipse highlights the strongest response from the low-velocity zone overlying the subducting slab. Lastly, (c) earthquake epicenters within 20 km of the MASE array projected onto the image. The locations are from the Servicio Sismológico Nacional catalog. For reference, Mexico City's relative position projected onto the plane of the profile is denoted by the blue house at the top of each panel. The Chichinautzin volcanic field is denoted with the red triangle.

30 km of depth, we increase shear wave velocities from 3200 m/s to 3600 m/s. At 40 km depth, we apply 4400 m/s and increase to 4700 m/s by 400 km depth.

4.1. Interpretation and Discussion

The migrated depth image is given in Figure 10. Station offset refers to projected linear distance from the southernmost receiver position near Acapulco. Positive polarities are denoted in red. Through the interferometric processing, the actual reflectivity is overlain by a zero-phase wavelet. Hence, a positive velocity contrast (increase in velocity with depth) is imaged as a red feature with small blue sidelobes. The actual interface is located on the crest of the red zero-phase wavelet. Due to the relatively low frequencies retrieved and the presence of sidelobes, we focus our interpretation on high-amplitude features. In the first lateral 80–100 km of the profile, we note the steady dip of a strong positive reflector beginning at 30 km depth ending at 50 km depth. We interpret this dipping feature as the subducting oceanic crustal slab, where the angle of dip and position is in agreement with the previous observations by *Pérez-Campos et al.* [2008] and *Kim et al.* [2012]. Beyond this region of gentle dip, the slab flattens and remains horizontal for a significant lateral distance. This horizontal region spans from approximately 80 km to 200 km offset from

the first station. This section corroborates existing literature noting the horizontal nature of the slab in this region [e.g., *Pérez-Campos et al.*, 2008, *Chen and Clayton*, 2009; *Kim et al.*, 2012]. The strong negative reflector underpinning the subducting slab between approximately 120 and 200 km station offset may be the bottom of the slab. At 200 km station offset, the horizontal migration ceases, and for the next 50 km, the slab signature begins to dip again. By 60 km depth and 250 km offset, the subducting slab disappears entirely from the image. Beyond this region, the slab is expected to plunge steeply into the mantle. Dip values of 70 to 80° are commonly cited from tomography studies such as those in *Pérez-Campos et al.* [2008] and *Husker and Davis* [2009].

At 200 km from the first seismometer station, a fork in the positive reflector occurs. In the previous paragraph, we interpret this region to be where the subducting slab begins dipping into the mantle. At larger station offsets, the continental crust overlays the upper mantle, resulting in a positive reflection at the Moho. In the reflectivity image, the Moho interface reaches a maximum depth of about 45 km near 250 km station offset and undulates to 35 km depth near 400 km station offset, which agrees closely with depths cited in *Pérez-Campos et al.* [2008] and *Kim et al.* [2012]. The northward thinning of the continental crust is in agreement with gravity-derived observations based on data from the European Space Agency's Gravity field and Ocean Circulation Explorer (http://facility.unavco.org/software/idv/IDV_datasource_Moho.html). The lack of any discernible continental root below the Trans-Mexican Volcanic Belt (TMVB, which spans from 250 to 400 km offset) is in agreement with *Kim et al.* [2010].

An interesting feature occurs at approximately 70 km station offset and 40 km depth. A strong negative reflector (imaged with blue) is noted, immediately below which the subducting slab (imaged with red) ceases its shallow dip and transitions to near horizontal. We interpret the region in between the blue and red reflector as the LVZ. From RFs, the same zone was inferred [*Kim et al.*, 2010]. Numerical modeling in *Manea and Gurnis* [2007] shows how a low-viscosity zone (produced, e.g., by dehydration of a subducting slab) is capable of transitioning a dipping subduction zone into a flat one. The apparent sag of the horizontal slab immediately below this feature is likely nonphysical but rather a velocity effect, since a one-dimensional velocity model was used for location of the reflectivity. Additionally, the strength of the negative reflector likely interferes with the reflection from the underlying plate, slightly exaggerating the apparent sag.

Following the horizontal slab beyond this point, the signal of the well-defined LVZ reflection weakens. Existing studies (e.g., *Manea and Gurnis* [2007] and *Kim et al.* [2010]) indicate a larger lateral extent for the LVZ than is observed in our retrieved image. In our technique, maximum amplitudes are retrieved at the location of maximum velocity and density contrast. The maximum imaged thickness of this LVZ (15 km) could sustain flat subduction, given a low viscosity [*Manea and Gurnis*, 2007]. According to the recent observations in *Kim et al.* [2013], the LVZ is found to be as thin as 4 km in some spots. We expect that the LVZ continues beyond the strong negative reflector noted in our image, but the detected and exploited *S* waves lack the required bandwidth to image features as thin as 4 km. Finally, at approximately 200 km, the horizontally migrating slab is no longer visible and either dips steeply into the mantle or is no longer present.

We also create a figure that overlays the Servicio Sismológico Nacional catalog of earthquake epicenters within 20 km of the MASE array occurring within the last 40 years atop our migrated image. Apparent clusters of earthquakes form in several locations; along the span of the coastal region, a deeper cluster at 50–60 km depth and 75–150 km station offset, and a final cluster in the shallow subsurface near Mexico City. The locations near the coast correspond to the beginning of the subduction zone where the subducting plate is forced below the overriding continental crust. The final cluster occurs in the shallow reaches of the TMVB where intrusions in the upper crust cause seismicity. The location of the central cluster shows a less familiar character. This cluster occurs near the region where plate motion has transitioned into a horizontal plane. The depths of these quakes, in almost all cases, are located either below the LVZ, or above the LVZ, supporting the existence of a low strength layer devoid of seismicity. A number of the quakes also appear to locate within the subducting slab itself. Please be aware that while the latitude and longitude locations of earthquake hypocenters are typically quite accurate, there could remain considerable uncertainty, especially in depth. Whether events such as these are related to the dehydration process of a subducting slab itself or some other mechanism is an area of ongoing research and debate [*Ranero et al.*, 2003; *Hacker et al.*, 2003a; *Hacker et al.*, 2003b; *Abers et al.*, 2009]. Nonvolcanic tremors occur mostly at depths situated in the continental crust above the LVZ imaged here [*Payero et al.*, 2008].

Finally, we discuss the overall image quality. One of the advantages of applying teleseismic SI for imaging purposes is to retrieve reflectivity information from subsurface without needing a priori knowledge of the geological environment. For this to be achieved, the most important criterion is a good approximation of the interferometric integral (equation (2)). A good approximation is achieved with a collection of regularly sampled (in the ray parameter domain) phase responses. More detailed sampling requirements are elaborated in *Ruigrok et al.* [2010]. In the case of the MASE field data set, the sampling available falls short of the ideal sampling scenario demonstrated in the 2-D modeling. The actual ray parameters sampled by the field data set are included in Figure 1c. The lack of regular sampling is primarily due to the orientation of the array, which was not in-line with any seismically prolific region, rather than any net shortage of earthquakes occurring during the entirety of the MASE recording interval. A consequence of this uneven sampling resulted in us using only the zero-offset reflections for the final imaging stage. If also the nonzero-offset reflections had been of good quality, an image with an improved signal-to-noise could have been obtained. Moreover, a velocity model could have been estimated directly from the retrieved reflections. Other seismometer arrays were considered for this application, but the alternative candidates had large station intervals (where spatial aliasing would have been a risk), were active for shorter durations, or also demonstrated a nonideal orientation. Despite these obstacles, the technique is still capable of highlighting subsurface details with interpretive value, as demonstrated in our modeling section and field data results.

5. Conclusions

We showed that a shear wave reflectivity image can be obtained by combining seismic interferometry with seismic reflection imaging. The reflectivity is retrieved from the coda of *S* wave transmission responses due to distant seismicity. Structural information is delineated directly below an array of seismometers. A drawback to the technique presented is that a well-sampled data set (with a regular distribution of ray parameters) is required in order to produce a high-resolution image of the subsurface. However, we showed both with synthetic and field data that large lithospheric features are still resolved with the suboptimal source sampling. Also, we showed that spurious events caused by long source-time functions can largely be suppressed by filtering in the common-offset domain, although at the cost of marginally suppressing horizontal structure. Applying the presented technique to future data sets, and more specifically, with arrays designed to apply teleseismic shear wave SI, may reveal details that unlock further knowledge relating to lithosphere geometry and development.

References

Abers, G. A., L. S. MacKenzie, S. Rondenay, Z. Zhang, A. G. Wech, and K. C. Creager (2009), Imaging the source region of Cascadia tremor and intermediate-depth earthquakes, *Geology*, *37*(12), 1119–1122.

Bostock, M., S. Rondenay, and J. Shragge (2001), Multiparameter two-dimensional inversion of scattered teleseismic body waves. 1. Theory for oblique incidence, *J. Geophys. Res.*, *106*(B12), 30,771–30,782.

Chen, T., and R. W. Clayton (2009), Seismic attenuation structure in central Mexico: Image of a focused high-attenuation zone in the mantle wedge, *J. Geophys. Res.*, *114*, B07304, doi:10.1029/2008JB005964.

Contreras-Reyes, E., J. Jara, I. Grevemeyer, S. Ruiz, and D. Carrizo (2012), Abrupt change in the dip of the subducting plate beneath north Chile, *Nat. Geosci.*, *5*(5), 342–345.

Derode, A., E. Larose, M. Tanter, J. de Rosny, A. Tourin, M. Campillo, and M. Fink (2003), Recovering the Green's function from field-field correlations in an open scattering medium, *J. Acoust. Soc. Am.*, *113*, 2973–2976.

Draganov, D., K. Wapenaar, and J. Thorbecke (2006), Seismic interferometry: Reconstructing the Earth's reflection response, *Geophysics*, *71*(4), SI61–SI70.

Dziewonski, A. M., and D. L. Anderson (1981), Preliminary reference Earth model, *Phys. Earth Planet. Inter.*, *25*(4), 297–356.

Hacker, B. R., S. M. Peacock, G. A. Abers, and S. D. Holloway (2003a), Subduction factory. 2. Are intermediate-depth earthquakes in subducting slabs linked to metamorphic dehydration reactions?, *J. Geophys. Res.*, *108*(B1), 2030, doi:10.1029/2001JB001129.

Hacker, B. R., G. A. Abers, and S. M. Peacock (2003b), Subduction factory. 1. Theoretical mineralogy, densities, seismic wave speeds, and H_2O contents, *J. Geophys. Res.*, *108*(B1), 2029, doi:10.1029/2001JB001127.

Husker, A., and P. M. Davis (2009), Tomography and thermal state of the Cocos plate subduction beneath Mexico City, *J. Geophys. Res.*, *114*, B04306, doi:10.1029/2008JB006039.

Kennett, B. (1991), The removal of free surface interactions from three-component seismograms, *Geophys. J. Int.*, *104*(1), 153–154.

Kim, Y., R. Clayton, and J. Jackson (2010), Geometry and seismic properties of the subducting Cocos plate in central Mexico, *J. Geophys. Res.*, *115*, B06310, doi:10.1029/2009JB006942.

Kim, Y., M. S. Miller, F. Pearce, and R. W. Clayton (2012), Seismic imaging of the Cocos plate subduction zone system in central Mexico, *Geochem. Geophys. Geosyst.*, *13*(7), Q07001, doi:10.1029/2012GC004033.

Kim, Y., R. W. Clayton, P. D. Asimow, and J. M. Jackson (2013), Generation of talc in the mantle wedge and its role in subduction dynamics in central Mexico, *Earth Planet. Sci. Lett.*, *384*, 81–87.

Lobkis, O., and R. Weaver (2001), On the emergence of the Green's function in the correlations of a diffuse field, *J. Acoust. Soc. Am.*, *110*, 3011–3017.

FRANK ET AL.
13

Manea, V., and M. Gurnis (2007), Subduction zone evolution and low viscosity wedges and channels, *Earth Planet. Sci. Lett.*, *264*(1), 22–45.

MASE (2007), Meso-America Subduction Experiment, *Caltech. Dataset*, doi:10.7909/C3RN35SP.

Payero, J. S., V. Kostoglodov, N. Shapiro, T. Mikumo, A. Iglesias, X. Pérez-Campos, and R. W. Clayton (2008), Nonvolcanic tremor observed in the Mexican subduction zone, *Geophys. Res. Lett.*, *35*, L07305, doi:10.1029/2007GL032877.

Pérez-Campos, X., Y. H. Kim, A. Husker, P. M. Davis, R. W. Clayton, A. Iglesias, J. F. Pacheco, S. K. Singh, V. C. Manea, and M. Gurnis (2008), Horizontal subduction and truncation of the Cocos plate beneath central Mexico, *Geophys. Res. Lett.*, *35*, L18303, doi:10.1029/2008GL035127.

Ranero, C., J. P. Morgan, K. McIntosh, and C. Reichert (2003), Bending-related faulting and mantle serpentinization at the middle America trench, *Nature*, *425*(6956), 367–373.

Ruigrok, E., and K. Wapenaar (2012), Global-phase seismic interferometry unveils P-wave reflectivity below the Himalayas and Tibet, *Geophys. Res. Lett.*, *39*, L11303, doi:10.1029/2012GL051672.

Ruigrok, E., X. Campman, D. Draganov, and K. Wapenaar (2010), High-resolution lithospheric imaging with seismic interferometry, *Geophys. J. Int.*, *183*(1), 339–357.

Snieder, R. (2004), Extracting the Greens function from the correlation of coda waves: A derivation based on stationary phase, *Phys. Rev. E*, *69*(4), 046610.

Stein, S., and M. Wysession (2009), *An Introduction to Seismology, Earthquakes, and Earth Structure*, Wiley-Blackwell, New York.

Thorbecke, J. W., and D. Draganov (2011), Finite-difference modeling experiments for seismic interferometry, *Geophysics*, *76*(6), H1–H18.

Verschuur, D., and A. Berkhout (1997), Estimation of multiple scattering by iterative inversion. Part II: Practical aspects and examples, *Geophysics*, *62*(5), 1596–1611.

Wapenaar, K. (2003), Synthesis of an inhomogeneous medium from its acoustic transmission response, *Geophysics*, *68*(5), 1756–1759.

Wapenaar, K., and J. Fokkema (2006), Green's function representations for seismic interferometry, *Geophysics*, *71*(4), SI33–SI46.

Wapenaar, K., J. Thorbecke, and D. Draganov (2004), Relations between reflection and transmission responses of three-dimensional inhomogeneous media, *Geophys. J. Int.*, *156*, 179–194.

Wapenaar, K., D. Draganov, R. Snieder, X. Campman, and A. Verdel (2010a), Tutorial on seismic interferometry. Part 1: Basic principles and applications, *Geophysics*, *75*(5), 75,A195–75,A209.

Wapenaar, K., E. Slob, R. Snieder, and A. Curtis (2010b), Tutorial on seismic interferometry. Part 2: Underlying theory and new advances, *Geophysics*, *75*(5), 75,A211–75,A227.

Yilmaz, O. (2001), *Seismic Data Analysis*, Society of Exploration Geophysicists, Tulsa, Okla., doi:10.1190/1.9781560801580.